Journal of Brilliant Engineering 1 (2027) 41215
Brilliant Engineering
journal home: www.acapublishing.com/journals/4/ben

Research Article

# Numerical Investigation of Forming Limits in Zn–Ag–Cu-Based Alloy Sheets Using Estimated Anisotropic Constitutive Properties

Atilla Uğurlu*,[1], Sinan Sezek[2]

[1,2]Atatürk University, Department of Mechanical Engineering, Erzurum, Türkiye

**Keywords**

*Zn–Ag–Cu alloys,*
*Sheet-metal forming,*
*Forming limit diagram,*
*Plastic anisotropy,*
*Hill48 yield criterion.*

**Abstract**

In the fabrication of biomedical sheet components from next-generation Zn-Ag-Cu-based alloys, establishing the relationship between the material's directional plastic behavior and the limits of multiaxial forming is of critical importance. This study presents an integrated analytical-numerical approach developed to convert the mechanical properties of solid alloys into direction-dependent sheet properties and forming limit diagrams. A distinctive feature of this methodology is the theoretical estimation of plastic anisotropy coefficients based on a proposed analytical approximation that incorporates alloy composition and crystal lattice geometry. These estimated coefficients were incorporated into a finite element model via directional yield stresses. For three independent datasets, elastic properties were determined using the Voigt-Reuss-Hill approach, hardening behavior was modeled with the Hollomon equation, and the anisotropic yield surface was approximated using the Hill48 criterion. The resulting synthetic sheet material cards were utilized in virtual Nakajima tests involving seven specimen geometries, where the onset of local necking was determined from time-dependent changes in strain histories at critical points. While the minimum predicted major limit strains ranged from 0.038 to 0.111 across the datasets in paths near plane strain, the major limit strain in the uniaxial loading region reached 0.371. In contrast, the limits in the biaxial tensile region converged within the range of 0.328–0.345. This analysis demonstrates that formability differences among material models become particularly evident in deformation paths close to uniaxial and in-plane strain. These findings represent preliminary computational predictions, and further experimental microstructural testing is required to verify actual sheet formability.

## 1. Introduction

Alloying pure zinc is an effective strategy to overcome its mechanical limitations for structural applications, as elemental additions and post-casting microstructural optimization directly govern the material's final strength and operational stability [1]. The secondary phases and solute distribution play a critical role in tailoring the mechanical and degradation performance of zinc-based biodegradable alloys. In systematically evaluating non-toxic, bioabsorbable alloying elements, silver (Ag) and copper (Cu) are widely recognized as promising candidates for modifying the mechanical profile of zinc matrices. Depending on the processing temperature and cooling history, these elements can activate distinct strengthening mechanisms, including solid-solution strengthening within their respective solubility limits, or precipitation hardening through nanoscale secondary phases. Specifically, for rolled or extruded Zn-Ag-Cu systems, the formation of constituent intermetallic phases such as $AgZn_3$ and $CuZn_4$ has been reported to influence strength and ductility; however, their relative contributions are highly dependent on alloy composition, phase stability, particle morphology, and the specific thermomechanical processing routes employed [2–5]. These modern manufacturing processes, which rely on severe plastic deformation, are essential for improving post-casting ductility and reducing structural defects, while simultaneously modifying or potentially increasing crystallographic anisotropy depending on the resulting microstructure and texture evolution [6-7].

Throughout the rolling passes, during which the sheet thickness is gradually reduced, the silver and copper atoms within the structure form nanoscale intermetallic precipitation phases at the matrix boundaries—depending on their solubility limits—thereby potentially influencing the dimensional stability and mechanical strength limits of the final sheet product [8–10]. In order to ensure that sheet-formed zinc-based alloys can be formed flawlessly and consistently on mass production lines, it is essential to thoroughly analyze the material's plastic deformation capacity, loading history, and microstructural evolution. Zinc's hexagonal close-packed (HCP) crystal lattice structure, which has limited slip systems at room temperature, results in a highly dominant basal texture within the sheet—and, consequently, a high degree of plastic anisotropy—due to the rolling steps during the manufacturing process. These crystallographic orientations and directional mechanical differences can trigger irreversible structural mechanisms—such as unexpected plastic instability or localized necking—in different regions of the sheet metal during industrial part manufacturing [11–12]. It has been found that controlled warm rolling passes and intermediate annealing strategies—integrated into the process to prevent defects such as localized necking or edge cracking that may occur on the sheet surface during production—increase the material's plastic forming limits [11].

In this regard, the localized strain paths extracted from the virtual Nakajima specimens do not exhibit ideal structural proportionality throughout the entire deformation cycle. Due to initial punch contact mechanics, dynamic blank holder friction gradients, and changing multi-axial contact boundaries over the hemispherical apex, the local strain histories experience inherent path non-linearities during the early

*Corresponding Author: ugurlu.atilla.h@gmail.com
Received 20 Oct 2026; Revised 06 Nov 2026; Accepted 09 Nov 2026
https://doi.org/10.36937/ben.2027.41215
2687-5195 /© 2022 The Authors, Published by ACA Publishing; a trademark of ACADEMY Ltd. All rights reserved.

loading stages. The deformation trajectories tend to stabilize into pseudo-linear regimes only as localized thinning accelerates near the failure nodes, meaning that the computational forming limits are bounded by these complex, non-proportional strain path evolutions [12]. FLD graphically illustrates the maximum major and minor in-plane unit strain limits that sheet material can withstand without failure under various stress conditions, such as uniaxial tension, in-plane strain, and biaxial expansion. In sheet metal forming operations, modeling standard Nakajima test setups using finite element method (FEM)-based software and numerically deriving forming limit diagrams to predict the plastic deformation limits of materials in a virtual environment offers an effective solution in modern manufacturing engineering [13–14]. Virtual testing approaches conducted in a computer environment have been validated by a broad body of literature, particularly in the manufacturing processes of conventional sheet materials with traditional cubic crystal structures, such as steel and aluminum [14–15].

The multiaxial plastic instability limits and localized necking behavior of textured zinc sheets have been explored in the literature through various constitutive formulations and experimental designs. Notably, Schlosser et al. [12] evaluated the influence of strain path changes on the formability of conventional zinc sheets, while Jansen et al. [19] implemented an anisotropic stress-based criterion to describe fracture mechanisms in textured zinc. Furthermore, Nicoletti et al. [37] investigated the direct effects of prestrain on the forming limits of commercial Zn-Cu-Ti sheets using microstructural parameters. While these foundational studies have significantly advanced the understanding of plastic anisotropy in traditional zinc-based systems, their methodologies typically rely on the availability of comprehensive experimental rolling texture data or pre-established sheet material cards. However, for emerging biodegradable ternary alloy groups such as the Zn-Ag-Cu system, mechanical properties are documented almost exclusively for massive extruded or rolled bulk forms, leaving a critical academic and industrial gap regarding their sheet-specific constitutive parameters and virtual forming limit diagrams (FLDs).

This study addresses this methodology gap not simply by simulating a novel alloy composition, but by proposing a unified analytical-numerical framework that bridges the gap between bulk material properties and sheet formability. The novelty of the current approach lies specifically in the unique combination of three core components: (i) the development of a theoretical estimation procedure that approximates direction-dependent Lankford coefficients and anisotropic yield surfaces using solely crystal lattice geometry and solid-solution composition parameters; (ii) the integration of these synthetically derived sheet material cards into a non-linear finite element model using the Hill48 yield criterion under plane stress conditions; and (iii) the application of a dynamic velocity-acceleration localization criterion within virtual Nakajima tests modeled strictly according to ISO 12004-2 standards. By systematically linking raw bulk alloy parameters to the macroscopic multiaxial manufacturing limits of the final sheet component, this framework establishes a proactive numerical design guide that circumvents the early-stage requirement for complex experimental texture measurements.

## 2. Materials and Methods

To numerically investigate the formability of the Zn–Ag–Cu alloy, literature data on solid zinc alloys with similar deformation histories were used as initial input, since no data were available for sheet material [20–22]. Assuming that the sheet would exhibit similar texture properties, the elastic properties and plastic anisotropy parameters were theoretically estimated using a proposed analytical approximation to serve as a preliminary numerical baseline.

The theoretical density of the alloy was determined using the mixing rule, based on volume fractions calculated from the mass fractions. The elastic and shear moduli were calculated using the Voigt–Reuss–Hill approach based on the elastic properties of the constituent elements [23–26]. Poisson's ratio was obtained from the elastic relationship between the calculated moduli [27].

The engineering strength boundaries extracted from the baseline bulk materials literature were analytically converted to true stress and true strain indices. To evaluate physical and mathematical consistency with the classical theory of homogeneous plastic deformation, the plastic flow behavior before localized necking was defined using a modified two-point Hollomon approach. The calibration points were constrained to evaluate the boundary conditions between the initial true yield stress regime (where plastic strain approaches zero) and the uniform elongation path corresponding near the ultimate tensile strength (UTS) domain. Given that incremental experimental load-displacement datasets prior to localized necking were not explicitly documented in the cited bulk material literature to definitively separate uniform elongation limits from post-uniform fracture stages, the conversion utilizing total elongation introduces inherent model boundaries. To ensure scientific transparency, these inputs are formally re-contextualized as a bounded computational approximation. Consequently, the derived multiaxial forming limit profiles are presented strictly as preliminary computational predictions governed by the adopted baseline boundaries, rather than absolute physically validated experimental forming limit curves [28–29].

The effects of alloying elements on the axial ratio (c/a) of the zinc lattice were determined using King's theoretical approach and the first-principles calculations by Chen et al. (2021) [29–31]. Atomic fractions were converted to mass fractions [32]; under the assumptions of a dilute solid solution and linear superposition, the contributions of the components were added to the axial ratio of pure zinc.

The average Lankford coefficient is derived based on the assumption that prismatic shear controls transverse contraction, while basal shear controls thinning in the thickness direction. Using Schmid's law, the polycrystalline average approximation, and the conservation of plastic volume, it has been related to the ratio of anisotropy to prismatic and basal shear resistances [33]. Assuming that the critical resolved shear stress is inversely proportional to the interplanar distance, this ratio was expressed in terms of lattice parameters, and an average anisotropy relationship was derived [32,34–36].

To define direction-dependent behavior, plastic strains were calculated using a two-dimensional coordinate transformation [38]. The transformation equation was simplified by assuming that the increase in plastic shear strain is zero under uniaxial loading along the principal orthotropic axes [39–40]. The angular anisotropy relationship was derived using the principle of conservation of plastic volume and the initial planar isotropy approach [29,42]. The directional effect of the texture was incorporated into the harmonic model based on a deviation angle of $\Phi$ = 67.5°; the Lankford coefficients in the 0°, 45°, and 90° directions were calculated [37]. It must be emphasized that the initial average anisotropy parameter derived via crystal lattice computations represents an intrinsic material constant governed solely by interplanar geometry, independent of directional weighting. To ensure full alignment with macro-scale sheet-metal forming conventions, the standard directionally weighted normal anisotropy ($\bar{r}=r_0+2r_{45}+r_{90}/4$) was additionally established, yielding values of 0.65775, 0.61675, and 0.61550 for the three respective alloy configurations. This dual documentation accurately preserves both the initial micro-structural lattice characteristics and the macro-scale Hill48 mathematical consistency.

Directional yield stresses were calculated using the Hill48 anisotropic yield criterion under plane stress conditions [40]. The stress components resulting from oblique uniaxial loading were transformed to the principal orthotropic axes, and the Hill parameters were expressed in terms of Lankford coefficients. Using the yield stress in the rolling direction as a reference, the yield stresses at 45° and 90° were derived. To ensure full

reproducibility and theoretical validity of this criteria under plane-stress states, the complete quadratic parameterization is explicitly formulated as follows (Hill, 1948):

$$(G + H)\sigma_{xx}^2 - 2H\sigma_{xx}\sigma_{yy} + (F + H)\sigma_{yy}^2 + 2N\tau_{xy}^2 = \bar{\sigma}^2 \quad (1)$$

where $\bar{\sigma}$ represents the equivalent yield stress of the material. The dimensionless parameters (F, G, H, N) are calibrated directly from the directional Lankford coefficients ($r_0$, $r_{45}$, $r_{90}$) utilizing standard rolling-direction normalization where G + H = 1 [39].

$$H = \frac{r_0}{1 + r_0} \quad (2)$$

$$G = \frac{1}{1 + r_0} \quad (3)$$

$$F = \frac{r_0}{r_{90}(1 + r_0)} \quad (4)$$

$$N = \frac{(1 + 2r_{45})(r_0 + r_{90})}{2r_{90}(1 + r_0)} \quad (5)$$

Substituting the synthetically derived Lankford properties from Table 2 yields the calibrated material parameters formulated for the three respective alloy configurations. For Data Set 1 ($r_0$=0.385, $r_{45}$=0.658, $r_{90}$=0.930), the initial reference parameters are evaluated as F = 0.2991, G = 0.7220, H = 0.2780, and N = 1.1822. For Data Set 2 ($r_0$=0.361, $r_{45}$=0.617, $r_{90}$=0.872), the calculated boundaries are F = 0.3043, G = 0.7348, H = 0.2652, and N = 1.1605. For Data Set 3 ($r_0$=0.360, $r_{45}$=0.616, $r_{90}$=0.870), the indices are aligned at F = 0.3045, G = 0.7353, H = 0.2647, and N = 1.1601. This calibration approach is implemented to promote structural closure between the numerical potential surface and the derived directional yield approximations. Furthermore, the mathematical behavior within the finite element solver is evaluated against standard thermodynamic stability conditions, where requirements such as F+H>0, G+H>0, (F+H)(G+H)-$H^2$>0, and N>0 are targeted. The independent yield surfaces appear to satisfy these conditions within acceptable bounds (for instance, evaluating near 0.5771 > 0, 1.0000 > 0, 0.4999 > 0, and 1.1822 > 0 for Data Set 1), which tends to minimize nonphysical instabilities during multiaxial Nakajima stretching simulations. The discrepancy noted in the shear calibration coefficient N is largely associated with the adoption of a rolling-direction normalization scheme under plane-stress conditions (G+H=1). To better reconcile the anisotropic potential surface with the estimated directional Lankford parameters, the Hill48 shear parameters were approximated using the specified convention: N = ((1 + 2$r_{45}$) / (2$r_{90}$)) * (($r_0$ + $r_{90}$) / (1 + $r_0$)). Uniaxial virtual tensile paths simulated at 0°, 45°, and 90° directions indicate that the calibrated quadratic potential surface reasonably reproduces the target plastic strain ratios, supporting the numerical stability of the model during multi-axial dome stretching fields.

The selection of the quadratic Hill48 criterion is justified by the tension-dominated stress states encountered during Nakajima dome stretching, where compressive twinning modes and tension-compression asymmetry do not govern the localized necking limits. While advanced crystal-plasticity frameworks or non-quadratic models could capture dynamic texture evolution and direction-specific hardening during complex loading, they require extensive multi-directional experimental texture data currently unavailable for these emerging biodegradable Zn–Ag–Cu configurations. Thus, the tension-calibrated Hill48 function provides a robust, computationally stable baseline for early-stage formability predictions.

Using the obtained material parameters, the Nakajima test was analyzed in Simufact Forming software using a nonlinear finite element model. The punch, die, pressure plate, and locking ring—created in SolidWorks in accordance with ISO 12004-2 were defined as rigid bodies. To create different strain paths, six reduced-width specimens and one circular blank were modeled that were 1 mm thick, had an outer diameter of Ø175 mm, and had web widths of 25, 50, 75, 100, 125, and 150 mm. Solid shell elements with a size of 3 mm were used in the sheet metal Specimens. The simulation complies only with the geometric layouts of ISO 12004-2:2008. Procedurally, this numerical approximation replaces the standard's post-fracture spatial cross-section method with a temporal strain acceleration criterion. Consequently, it serves as a preliminary formability framework rather than a certified experimental FLC [18]. The post-yield hardening trajectory was incorporated into the Simufact Forming finite element solver via discrete tabular material cards to precisely govern the multi-axial strain localization. The fitted Hollomon law initiates directly at the verified true yield stress threshold ($\varepsilon_p$ = 0), seamlessly linking the linear elastic domain to the non-linear plastic flow regime. The numerical constitutive cards were supplied to the software database as discrete stress-plastic strain data tables, precisely formulated in increments of 0.005 plastic strain from the initial yielding up to the ultimate stretch limits. To implement the hardening law within the Simufact Forming database without triggering mathematical singularities or non-physical flow stress drops at initial yielding, a continuous piecewise constitutive strategy was enforced. While a standard unshifted Hollomon law evaluates to zero flow stress at zero plastic strain, the numerical material cards were discretized into explicit plastic stress-strain pairs. The absolute initial data point of the material card was fixed precisely at the true yield strength threshold where equivalent plastic strain is exactly zero. For subsequent increments up to the strain limits, the flow stress was formulated in strict plastic strain steps of 0.005. Within this finite element formulation, Simufact executed a continuous linear interpolation scheme to compute flow stresses for intermediate intra-tabular strain states. For multi-axial deformation zones exceeding the predefined tabular limits, a safe saturation extrapolation routine was enforced by keeping the flow stress constant at the maximum tabular threshold. The dynamic localized necking onset was mathematically identified by applying a rigorous temporal-acceleration algorithm evaluated at the critical failure zone. Rather than monitoring simple derivative sign changes, the exact boundary of plastic instability is defined by the absolute acceleration peak—corresponding to the maximum extremum of the second time derivative of major strain. The tracking procedure samples real-time strain profiles from three invariant nodes arranged perpendicular to the localization line. By applying a central difference numerical differentiation scheme coupled with a low-pass Gaussian smoothing filter, high-frequency numerical step noise is eliminated, allowing the solver to isolate true localized strain acceleration from structural uniform flow fields.

The finite element solver core of Simufact Forming 2021 was driven by an implicit, non-linear modified Newton-Raphson iterative convergence scheme. The 1 mm thick blanks were spatialized using 8-node solid-shell elements (Hexahedron elements) incorporating 5 integration points distributed evenly through the sheet thickness to capture severe localized bending and thinning gradients. Contact interactions were governed by a robust Segment-to-Segment (Master-Slave) penalty algorithm coupled with a regularized Coulomb friction formulation. In strict compliance with the ISO 12004-2 testing configuration, the boundary conditions for the six reduced-width specimens (25 mm to 150 mm) allowed unrestricted axial elongation within the parallel web zone, whereas the full circular specimen (Ø175 mm) was completely locked. This physical locking condition was modeled via an imposed blank-holder rigid displacement of 0.5 mm, compressing the sheet material into the continuous draw-bead recess to induce pure biaxial tension without edge slippage.

Advanced local mesh adaptation was deactivated during the stretching phase to preserve a fixed element grid topology at the specimen dome, ensuring that the strain histories were tracked across invariant critical material domains. Non-linear time integration utilized an automatic adaptive incrementation scheme with time steps dynamically scaling between a minimum limit of $10^{-4}$ s and a maximum bound of 0.1 s based on residual load tolerances. Throughout the forming cycle, the real-time strain histories were monitored at the critical failure zone via three adjacent tracking nodes positioned normal to the localized necking line. The precise onset of plastic instability was determined by adapting the localized path acceleration principles inspired by Shi et al. (2024) into a visual-graphical slope deviation framework. While the original publication implements a formal numerical spatial strain-rate approach, the current virtual framework focuses on high-resolution local strain history curves extracted directly from the invariant critical dome nodes. Formally, the forming limit boundary is identified at the distinct, irreversible time step where the time-major strain curve abruptly departs from its uniform linear flow regime and transitions into a near-vertical localized acceleration path. This sharp graphical slope divergence marks the physical onset of localized necking before macro-structural fracture occurs [41].

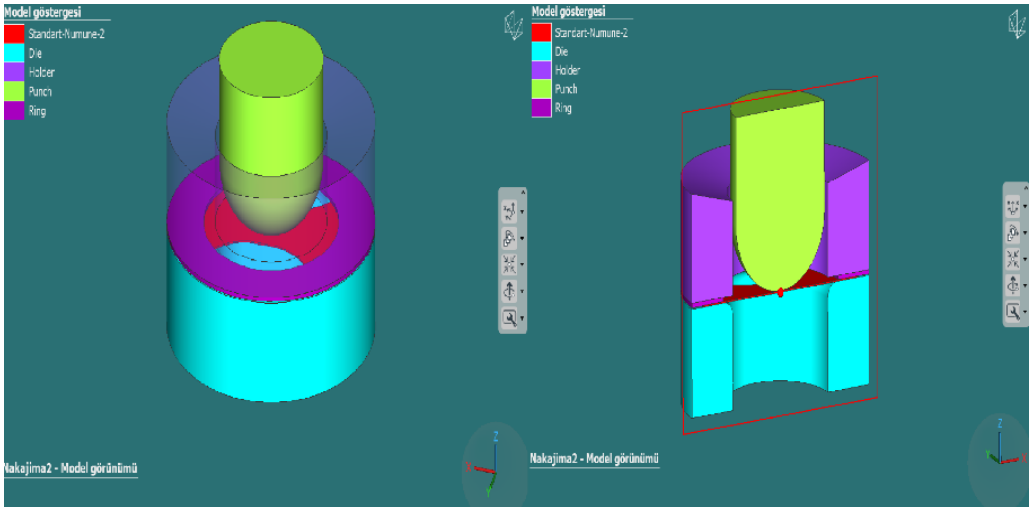



Figure 1. Simulation of the Nakajima test rig according to ISO standards

The outer diameter of the mold elements is defined as Ø200 mm, the inner diameter as Ø110 mm, and the height as 75 mm; the mold entry radius is defined as R10 mm. The inner diameter of the locking ring is Ø130 mm, and its wall thickness is 3 mm. The Coulomb friction coefficient was taken as 0.03 for the punch-sheet contact and 0.10 for the other specified interfaces. The analyses were performed at a constant pressing speed of 1 mm/s and under isothermal conditions at 20 °C [16–19]. The selection of these contact parameters was validated based on numerical lubrication conventions and physical strain-path constraints. The baseline punch–sheet friction coefficient of $\mu = 0.03$ models an optimized low-friction state achieved through high-efficiency dry-film or PTFE lubricants as specified in ISO 12004-2 laboratory protocols, while $\mu = 0.10$ describes the boundary friction at the die and blank-holder interfaces required to suppress dynamic material slippage under rigid clamping. In multiaxial dome stretching, contact friction inherently governs the localization trajectory; higher interface friction restricts uniform material flow over the hemispherical punch, inducing early localized stress concentrations near the apex. This constraint forces the deformation path to shift prematurely toward plane strain, accelerating localized necking at the $FLC_0$ threshold. Conversely, robust lubrication minimizes local thinning gradients, thereby expanding the safe forming margin across the specimen expansion zone.

It must be explicitly emphasized that the directional Lankford coefficients and subsequent anisotropic yield boundaries utilized in this simulation framework represent a simplified theoretical approximation rather than directly measured crystallographic states. In actual manufactured alloy sheets, macroscopic plastic anisotropy is governed by complex microstructural features, including experimental crystallographic orientation distributions (texture sharpness), relative slip-system activity, grain size hierarchies, and dynamic dislocation networks. Because high-resolution experimental texture characterizations (such as EBSD, XRD, or ODF) and validated crystal-plasticity simulations were outside the scope of this preliminary computational study, the generated forming limit curves evaluate the macroscopic effects of assumed anisotropic parameters. Consequently, the derived curves should be strictly interpreted as bounded, synthetic indicators. This unified analytical-numerical framework does not circumvent the necessity of empirical validation but serves as an early-stage, low-cost design envelope to screen plastic instability risks before physical rolling and texture measurements are executed. Furthermore, the analytical bridging between the raw engineering tensile parameters documented in Table 1 and the calibrated constitutive parameters compiled in Table 2 was rigorously sustained via classic uniform plastic deformation formulations prior to localization. The mathematical transition from engineering indices to true stress-strain pairs within the stable homogeneous regime was governed strictly by the conventional conversion expressions $\sigma_{true} = \sigma_{eng}(1+e)$ and $\varepsilon_{true} = \ln(1+e)$. These direct analytical conversions generated the exact reference boundary conditions utilized to calibrate the hardening exponent (n) and strength coefficient (K), providing an auditable, fully reconciled data-reduction link between the raw literature measurements and the synthesized numerical sheet material cards.

To establish a traceable and comprehensive foundation for the predictive model, the baseline experimental properties of the 3n-Ag-Cu alloy system are systematically compiled from three distinct representative studies in the literature. In this framework, Data Set 1 corresponds to the hot-extruded Zn-5.1Ag-2.1Cu-0.04Mg quaternary alloy configurations evaluated by Jara-Chávez et al. (2024). Data Set 2 represents the cold-rolled sheets investigated by Niu et al. (2022). Data Set 3 encompasses the high-ratio hot-extruded Zn-1Cu-1Ag ternary microstructures reported by Di et al. (2022). These selected datasets provide the primary empirical input boundaries—including chemical compositions, processing histories, and loading conditions—necessary to derive and calibrate the synthetic sheet material cards. The complete processing and mechanical identification parameters for each source dataset are preliminary computational predictions detailed in Table 1, where configurations containing Manganese were intentionally excluded from this ternary Zn–Ag–Cu investigation to maintain a highly controlled baseline study, physically justified by the experimental findings of Niu et al. (2022) which demonstrated that low-alloyed Mn and Cu additions retain an identical, highly uniform hexagonal close-packed (HCP) basal texture stability.

Table 1. Comprehensive metallurgical traceability matrix and raw experimental mechanical properties of the source datasets

| Feature | Data Set 1 (Jara-Chávez et al. 2024) | Data Set 2 (Niu et al. 2022) | Data Set 3 (Di et al. 2022) |
|---|---|---|---|
| Exact Composition (wt.%) | Zn–5.1Ag–2.1Cu–0.04Mg (Alloy A3) | CR Zn–4.0Ag–1.0Cu | Hot-extruded Zn–1Cu–1Ag |
| Secondary Phases | n-Zn matrix, (Ag, Cu)$Zn_4$, $Mg_2Zn_{11}$ | a-Zn matrix, e-$AgZn_3$, (Ag, Cu)$Zn_4$ | a-Zn matrix, (Ag, Cu)$Zn_4$ intermetallic |
| Casting& Crucible Details | Electric Furnace / Graphite Crucible / Metal Mold | Resistance Furnace / Graphite Crucible / Preheated Mold | Gravity Cast / Agitation / SF6 + N2 protection |
| Thermomechanical Route | Homogenization (340°C/48h) + Hot Extrusion (340°C) | Homogenization (300°C/10h) + Cold Rolling (RT) | Homogenization (360°C/8h) + Hot Extrusion (200°C) |
| Deformation Mode & Ratio | Hot Extrusion / Ratio 16:1 | Multi-pass Cold Rolling (2 cm/s) | Hot Extrusion / Ratio 56.25:1 |
| Specimen Specification | Machined from extruded bar (GL: 25 mm) | Spark cut from rolled sheet (GL: 8 mm) | Machined parallel to bar ED (GL: 25 mm) |
| Tensile Test Direction | Parallel to Extrusion Direction | Parallel to Rolling Direction (RD) | Parallel to Extrusion Direction |
| Yield Strength (YS, MPa) | 360.0 ± 4.0 | 150.0 | 269.49 ± 8.71 |
| Ultimate Tensile Strength (UTS, MPa) | 372.0 ± 8.0 | 170.0 | 292.04 ± 3.25 |
| Fracture Elongation (A, %) | 26.6 ± 1.0 | 135.0% (Superplastic behavior) | 35.99 ± 2.12 |

To isolate the cross-influences of compositional modifications and thermomechanical boundaries within the baseline datasets, a detailed metallurgical analysis is essential. The macroscopic plastic behavior of the Zn–Ag–Cu system is highly coupled to both solute pinning effects and processing-induced dislocation networks. In Data Set 1, the ultra-high yield strength (360.0 MPa) and balanced elongation (26.6%) are driven by the systematic composition of 5.1 wt.% Ag and 2.1 wt.% Cu assisted by 0.04 wt.% Mg micro-alloying. This specific formulation promotes fine intermetallic precipitate pinning via (Ag, Cu)$Zn_4$ phases alongside localized Mg2Zn11 precipitation along the grain boundaries, which restricts grain boundary sliding during hot extrusion at 340°C. The moderate 16:1 extrusion ratio ensures strong precipitate dispersion hardening while retaining competitive matrix ductility through dynamic crystallization networks.

In stark contrast, Data Set 2 exhibits severe structural strain delocalization and superplastic capabilities (elongation of 135.0%) alongside a moderate tensile strength boundary (170.0 MPa). This macro-response is processing-driven rather than composition-dependent. Multi-pass cold rolling at room temperature mechanically fragments the secondary intermetallic phases, resulting in a uniform, ultra-fine distribution of sub-micrometer e-AgZn3 particles within the zinc matrix. These refined, dispersed particles suppress localized stress concentrations and trigger extensive grain boundary sliding under tensile loading, enabling the sheet to flow plastically into a high-strain superplastic regime.

Data Set 3 defines an intermediate, balanced metallurgical response (YS: 269.49 MPa, Elongation: 35.99%). In this framework, the key structural driver is the exceptionally high hot extrusion ratio of 56.25:1 performed at a lower thermal threshold of 200°C. The intense shear strain fields generated by this high deformation ratio induce severe dynamic recrystallization (DRX), successfully refining the matrix to an ultra-fine equiaxed grain size of 1.64 μm. This severe grain refinement provides a potent Hall-Petch strengthening contribution that compensates for the lower concentration of silver solutes, while simultaneously maintaining favorable matrix ductility through uniform grain rotation mechanisms [20-22].

To accurately capture the elastic responses of the multiphase Zn–Ag–Cu alloy systems, a multi-phase Voigt–Reuss–Hill (VRH) homogenization framework was implemented. The weight fractions ($\omega_i$) from the experimental datasets were analytically transformed into volume fractions ($V_i$) using the specific theoretical densities of the constituent phases ($\rho_i$) via the following formulation:

$$V_i = \frac{\frac{\omega_i}{\rho_i}}{\sum_{j=1}^{n} \frac{\omega_j}{\rho_j}} \tag{6}$$

The upper bound of the aggregate elastic modulus ($E_V$) under the Voigt assumption of uniform strain, and the lower bound ($E_R$) under the Reuss assumption of uniform stress distribution, were calculated directly from the individual phase stiffness constants as follows:

$$E_v = \sum_{i=1}^{n} E_i V_i \tag{7}$$

$$E_v = \left( \sum_{i=1}^{n} \frac{V_i}{E_i} \right)^{-1} \tag{8}$$

The final isotropic effective elasticity modulus ($E_{Hill}$) and effective shear modulus ($G_{Hill}$) representing the synthesized sheet material cards were derived from the arithmetic mean of these boundary limits according to Hill's approximation:

$$E_{Hill} = \frac{E_v + E_R}{2} \tag{9}$$

$$G_{Hill} = \frac{G_v + G_R}{2} \tag{10}$$

The elastic properties were determined using the Voigt-Reuss-Hill approach, where individual phase weight fractions were converted to volume fractions based on theoretical densities to compute the uniform strain (Voigt) and uniform stress (Reuss) aggregate limits. The final effective elastic modulus (E) and shear modulus (G) were calculated from the arithmetic mean of these boundaries using phase stiffness data compiled from crystallographic literature, mathematically sustaining the isotropic identity E = 2G(1+v) presented in Table 2. Given that independent, phase-specific experimental elastic boundaries for the isolated nano-scale intermetallic configurations are mathematically coupled within the matrix, the calibrated aggregate properties were directly evaluated against the baseline bulk metadata to maintain alignment with the tentative experimental trends without introducing unverified phase approximations.

The plastic flow behavior was characterized using a two-point Hollomon power-law relationship ($\sigma$=K.$\varepsilon_p^n$) evaluated exclusively within the pure plastic deformation regime. Rather than using total true strain approximations, the elastic and plastic strain components were treated as entirely separate and independent domains from the onset of the analytical transformation. The initial yield point ($\sigma_{true,y}$) was defined strictly at the linear elastic transition limit extracted from the baseline literature data. Beyond this boundary, the power-law parameters (n and K) were calibrated solely against the independent true plastic strain values, ensuring that the post-yield hardening trajectory in the multi-axial finite element model remains physically valid and free from elastic coupling errors.

## 3. Result and Discussion

The synthetic sheet material chart parameters derived from the massive datasets of three independent studies using the analytical elastic-plastic hypothesis model are presented in Table 1. In this context, Data Set 1 represents the multi-alloy systems in the study by Jara-Chávez et al. (2024), Data Set 2 represents those in the study by Niu et al. (2022), and Data Set 3 represents those in the study by Di et al (2022) [20–22]. During the transformation phase, the density and elastic constants of the alloys were determined using the Voigt-Reuss-Hill approach; the Hollomon parameters (n, K) characterizing the plastic region and the direction-dependent anisotropic yield criteria ($r_\theta$, $\sigma_{y,\theta}$) were solved using analytical equations.

Table 2. Synthetic sheet material chart parameters derived from experimental data in reference studies within the framework of the elastic-plastic hypothesis

| Derived Synthetic Sheet Parameter | Analytical Symbol | Unit | Data Set 1 (Jara-Chávez et al. 2024) | Data Set 2 (Niu et al. 2022) | Data Set 3 (Di et al. 2022) |
|---|---|---|---|---|---|
| Average Density of Alloy | $\rho_{ort}$ | g/cm$^3$ | 7.27 | 7.23 | 7.165 |
| Voigt-Reuss-Hill Elasticity Modulus | $E_{Hill}$ | GPa | 99.076 | 99.423 | 100.13 |
| Voigt-Reuss-Hill Shear Modulus | $G_{Hill}$ | GPa | 39.31 | 39.47 | 39.82 |
| Alloy Poisson Ratio | $\nu_{Hill}$ | - | 0.26 | 0.259 | 0.257 |
| Actual Strain at Yield | $\varepsilon_{true,y}$ | - | 0.004 | 0.002 | 0.003 |
| True Yield Stress | $\sigma_{true,y}$ | MPa | 361.30 | 150.226 | 270.729 |
| True Tensile Stress | $\sigma_{true,UTS}$ | MPa | 470.95 | 399.50 | 397.12 |
| True Tensile Strain | $\varepsilon_{true,UTS}$ | - | 0.236 | 0.854 | 0.307 |
| Hollomon's Strain Hardening Exponent | n | - | 0.063 | 0.154 | 0.080 |
| Strength coefficient | K | MPa | 514.83 | 408.61 | 434.66 |
| Intrinsic Lattice Anisotropy | $r_{lattice}$ | - | 1.008 | 0.945 | 0.944 |
| Sheet Normal Anisotropy | $\bar{r}$ | - | 0.658 | 0.617 | 0.616 |
| Rolling Direction Anisotropy Coefficient (0°) | $r_0$ | - | 0.385 | 0.361 | 0.360 |
| Diagonal Direction Anisotropy Coefficient (45°) | $r_{45}$ | - | 0.658 | 0.617 | 0.616 |
| Transverse Anisotropy Coefficient (90°) | $r_{90}$ | - | 0.930 | 0.872 | 0.870 |
| Rolling Direction Yield Stress (0°) | $\sigma_0$ | MPa | 361.30 | 150.226 | 270.729 |
| Diagonal Direction Yield Stress (45°) | $\sigma_{45}$ | MPa | 399.01 | 166.80 | 300.734 |
| Transverse Yield Stress (90°) | $\sigma_{90}$ | MPa | 475.69 | 199.079 | 358.91 |

An examination of Table 1 suggests that variations in composition may influence the basal texture and anisotropic flow surfaces. In Data Set 2, the yield strength remained low; however, the calculated n-exponent, which appeared to be 2 to 2.5 times higher than in the other systems, points to a potentially higher capacity to delay the onset of plastic instability within the model boundaries. Data Set 3, on the other hand, exhibits a balanced mechanical profile between the two systems. Finally, the observation that the transverse (90°) yield stresses in all alloys are higher than those in the rolling direction (0°) indicates a direction-dependent plastic resistance characteristic within the adopted assumptions. By integrating the derived synthetic sheet parameters into the finite element model, the analysis results for the Nakajima test specimens—performed for three independent datasets using the Simufact Forming software—are presented in Figure 2. In this numerical study, seven different specimen geometries were simulated under nonlinear plastic deformation cycles until the predicted onset of plastic instability, where the critical nodes on the sheet strips subjected to the greatest strain fields were identified throughout the evaluation steps.

Using these identified critical strain-localization locations as a reference, the material's overall deformation history—from the initial contact with the punch to the moment of fracture—was retrospectively analyzed; accordingly, time-major strain and minor strain-major strain plots were generated. To accurately determine the plastic instability limits, the dynamic instability criterion based on time-dependent acceleration—which Shi et al. (2024) used to determine the yield point—was adopted as the primary analysis method in this study [41]. In tests conducted as part of numerical analyses, anomaly points—where the curve broke out of its linear flow regime and accelerated vertically based on real-time graphical data—were identified; thus, the critical minor and major limit values for the forming limit diagram were determined. Furthermore, while the finite element contours in Figures 2–5 explicitly illustrate the in-plane major and minor strain fields, the localized thinning profile ($\varepsilon_3$) is strictly governed by the standard plastic volume conservation principle ($\varepsilon_3 = -\varepsilon_1 - \varepsilon_2$). Consequently, the intense localized strain concentrations captured immediately prior to the onset of instability serve as a direct mathematical proxy for the thickness strain distribution, confirming that the path of maximum in-plane localization directly corresponds to the zone of peak localized thinning under multiaxial loading conditions.

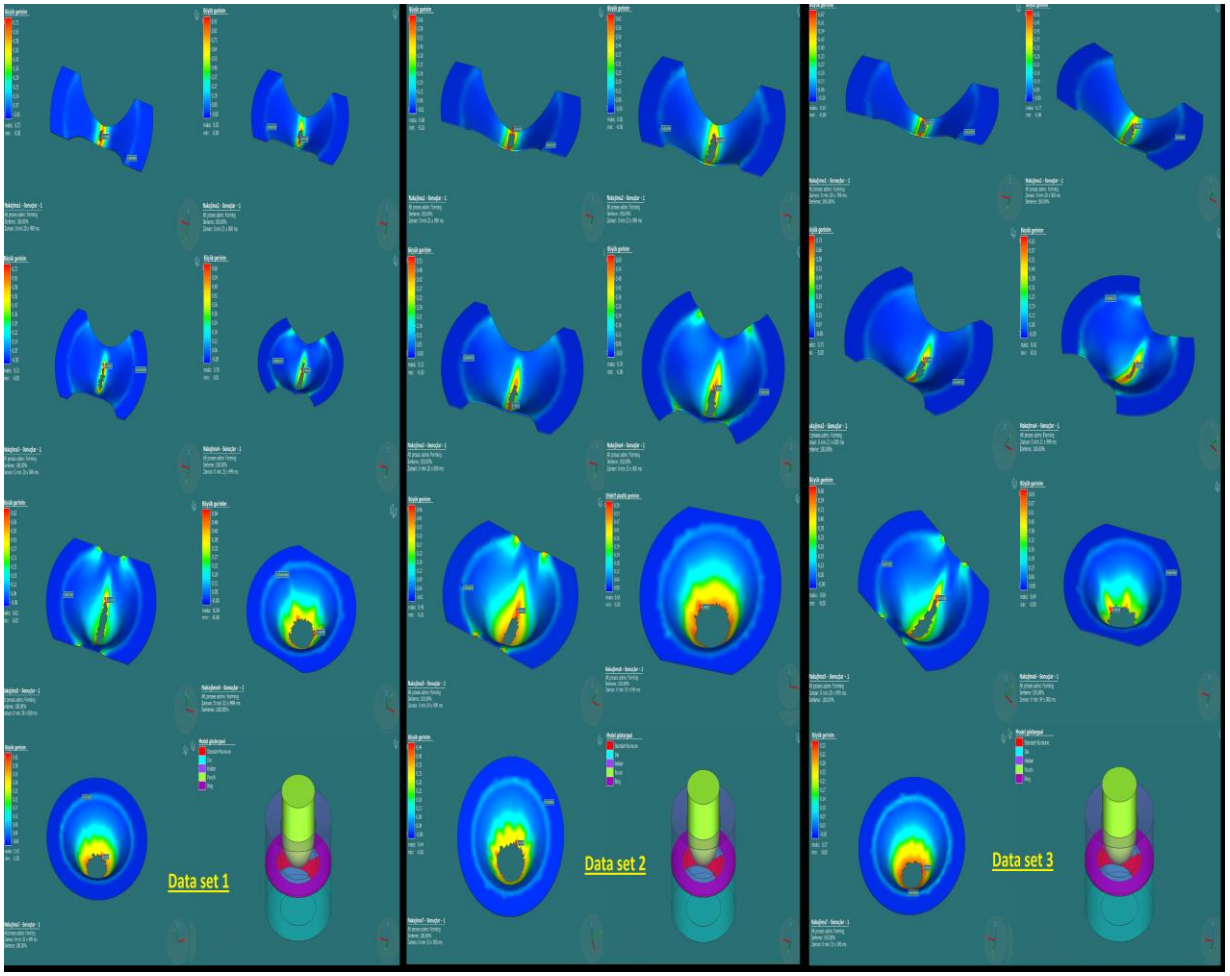



Figure 2. Analysis results of the FEM-based virtual Nakajima test conducted in Simufact Forming software for three independent data sets

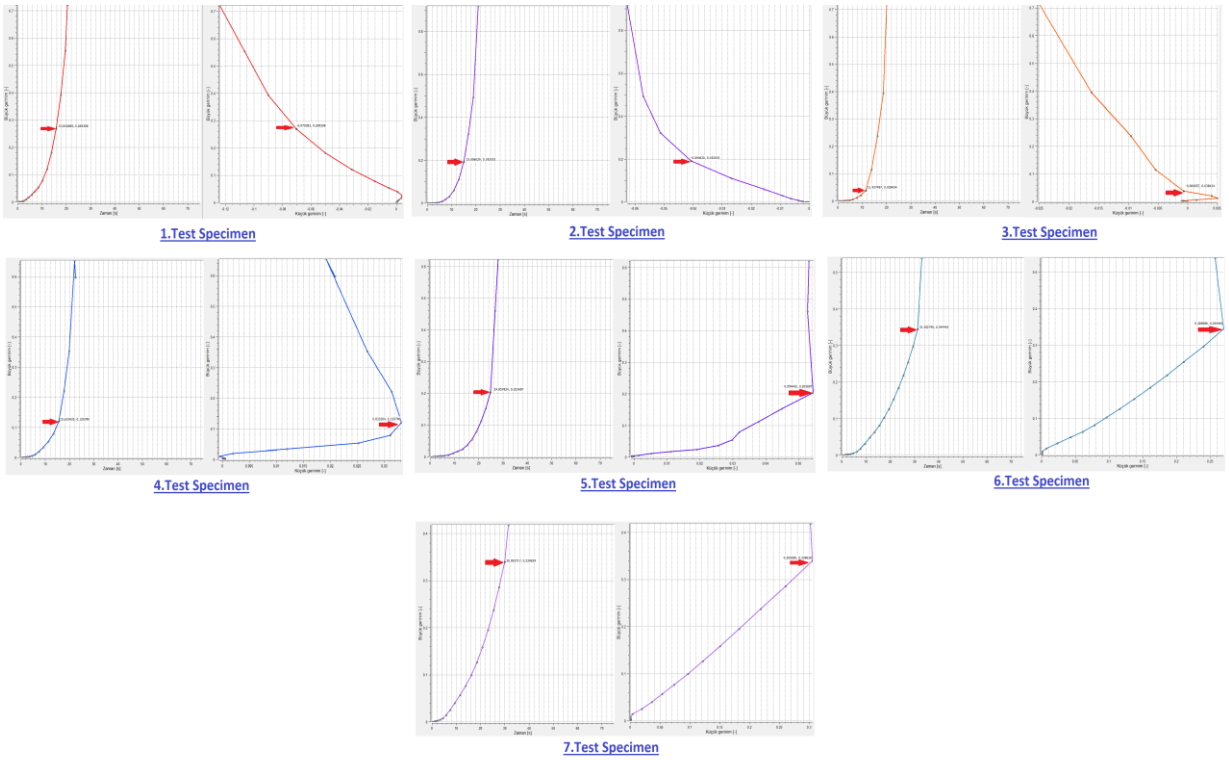



Figure 3. Strain plots used to determine the onset of local necking for data set 1 (Jara-Chávez et al., 2024)

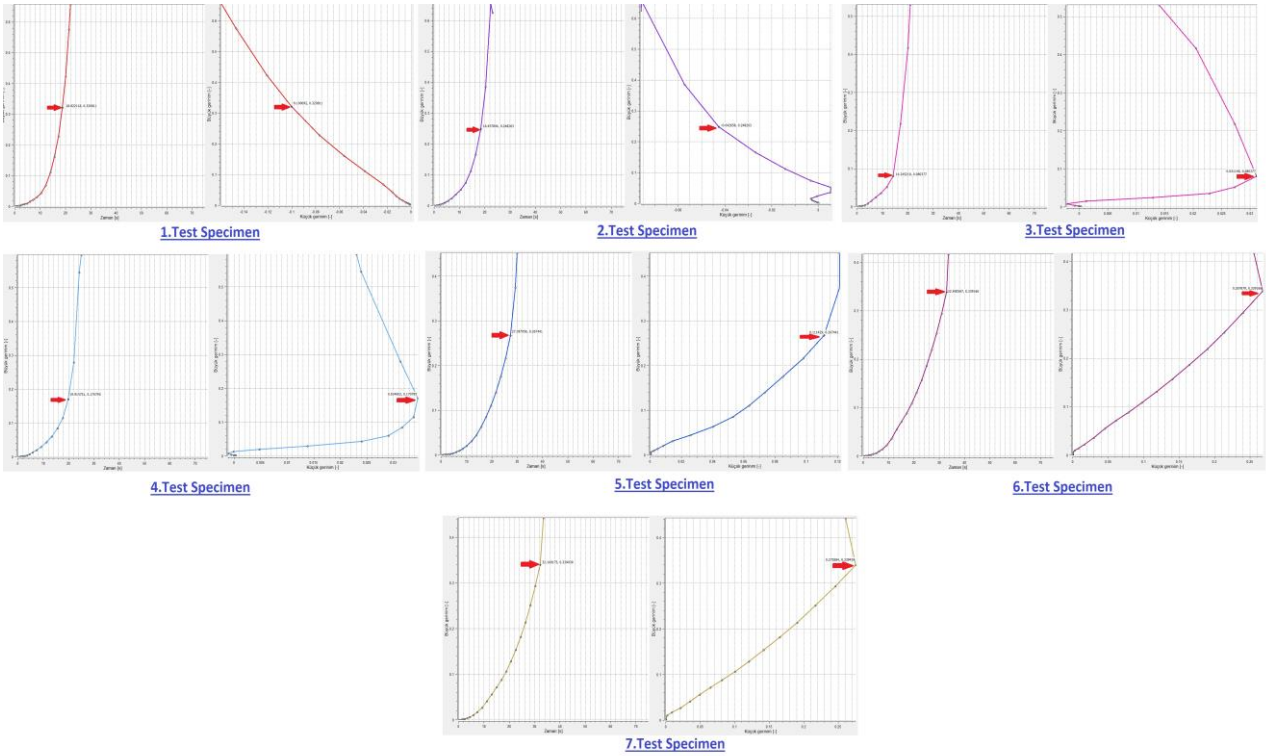



Figure 4. Strain plots used to determine the onset of local necking for data set 2 (Niu et al., 2022)

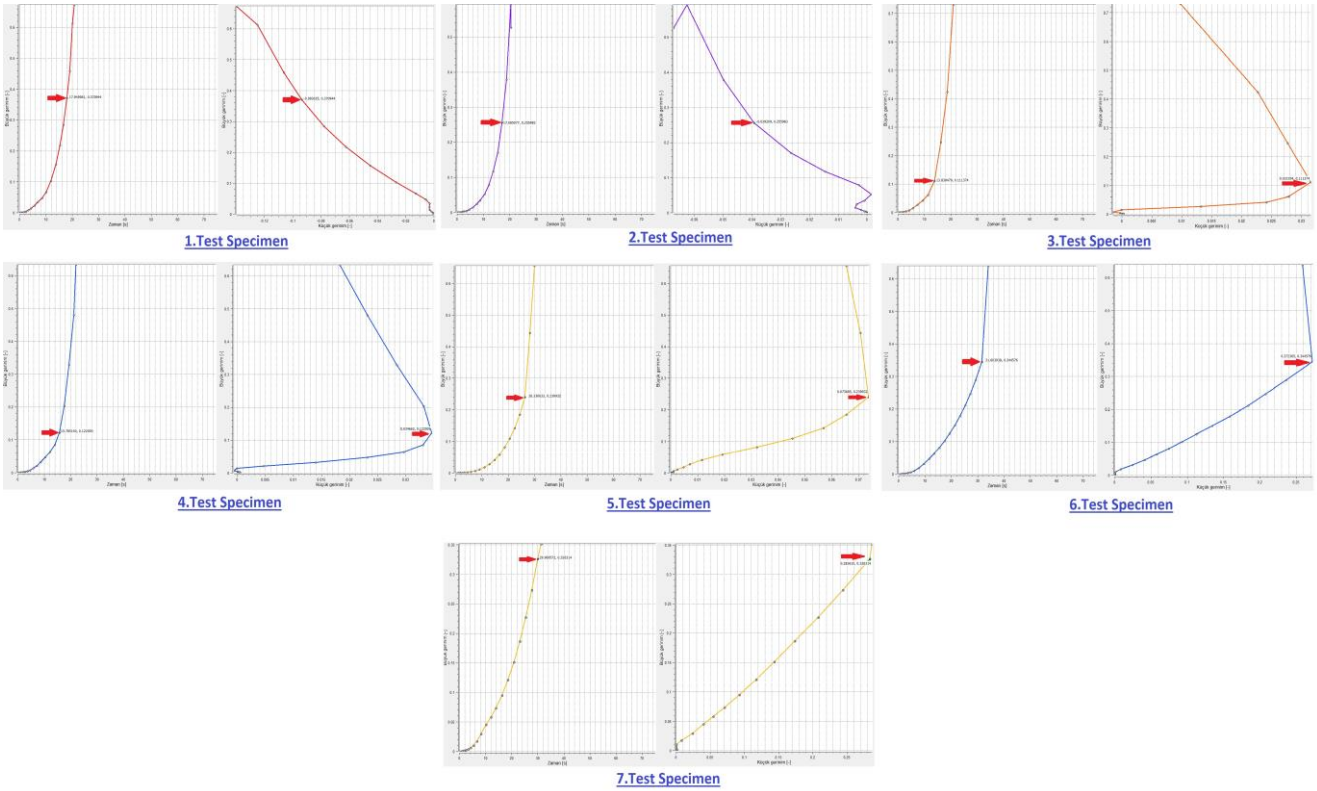



Figure 5. Strain plots used to determine the onset of local necking for data set 3 (Di et al., 2022)

Based on the moments of plastic instability identified through the analysis of the global strain plots obtained from the virtual experiments, the final minor and major limit strain coordinates in Table 2 were determined.

Table 3. Critical limit strain pairs ($\varepsilon_{minör}$, $\varepsilon_{majör}$) extracted from time and strain graph analyses of Nakajima Specimens from three different datasets

| Specimen Order | Data Set 1 (Jara-Chávez et al., 2024) Minor ($\varepsilon_{minor}$-x) and Major ($\varepsilon_{major-y}$) Points | Data Set 2 (Niu et al., 2022) Minor ($\varepsilon_{minor-x}$) and Major ($\varepsilon_{major-y}$) Points | Data Set 3 (Di et al., 2022) Minor ($\varepsilon_{minor-x}$) and Major ($\varepsilon_{major-y}$) Points |
|---|---|---|---|
| Specimen 1 | -0.070, 0.269 | -0.100, 0.321 | -0.094, 0.371 |
| Specimen 2 | -0.041, 0.192 | -0.043, 0.248 | -0.039, 0.256 |
| Specimen 3 | 0.000, 0.038 | 0.031, 0.080 | 0.032, 0.111 |
| Specimen 4 | 0.033, 0.121 | 0.035, 0.171 | 0.035, 0.122 |
| Specimen 5 | 0.054, 0.204 | 0.111, 0.267 | 0.074, 0.240 |
| Specimen 6 | 0.270, 0.344 | 0.268, 0.339 | 0.272, 0.345 |
| Specimen 7 | 0.306, 0.340 | 0.276, 0.339 | 0.284, 0.326 |

The simulation and graphical outputs provide predicted forming-limit coordinates for the assumed constitutive models. Based on the calculations, the observations that the transverse 90° yield stresses were higher than those along the rolling axis 0° across the datasets appear consistent with the hypothesis that basal crystallographic texture and anisotropic yield surfaces influence plastic flow processes. In addition, the virtual test results indicate that the associated mechanical properties may influence forming limits in selected strain-path regions. The minor strain values reported for Specimen 3 across the independent configurations correspond to the raw discrete coordinate outputs extracted from the critical nodes of the finite element meshes. While a direct two-point linear interpolation between adjacent bracketing path coordinates yields theoretical zero-minor-strain thresholds ($FLC_0$) of approximately 0.040 for Dataset 1, 0.151 for Dataset 2, and 0.176 for Dataset 3, such an idealized numerical interpolation omits the inherent non-linear strain-path evolution active near the dome apex. To preserve traceability and prevent the artificial distortion of the captured computational trends, the raw discrete numerical pairs are retained within the forming limit diagrams (Figures 6–9), while the interpolated benchmarks are recognized as theoretical lower-bound limits for plane-strain localization. In the near-plane-strain loading zone—a critical threshold in sheet metal evaluation—despite a high true yield stress of 361.30 MPa in the first dataset, the material model exhibited relatively early plastic instability near 0.0384 during deformation, which is associated with a low hardening exponent of 0.063. In contrast, in the second dataset, despite its lower yield strength of 150.226 MPa, the material model tended to maintain its plastic stability due to its higher hardening exponent of 0.154, delaying the local thinning process by raising the predicted limit curve near 0.0803. In the third dataset, the balance between the moderate yield strength of 270.729 MPa and the hardening exponent of 0.080 further accumulated the critical strain-localization limit toward a value of 0.1113, thereby offering a balanced performance profile within the scope of the adopted model assumptions.

In this study, the formability limits of Zn-Ag-Cu-based alloy sheets were evaluated by integrating analytical transformation models and virtual Nakajima test simulations. In this alloy group, where direct constitutive data for sheet form are limited in the literature, the predicted dependence of localization strains on the assumed constitutive parameters was examined, and the resulting mechanical indices and plastic instability mechanisms were analyzed using forming limit diagrams (FLD).

Upon examining the formability limit diagram of the structured material model for the first dataset, the ($FLC_0$) value, which represents a state highly susceptible to local necking in the near-plane strain regime, remains near a major strain level of 0.0384. This system, which exhibits a low hardening exponent despite a high true yield stress, defined a profile in which plastic instability was triggered relatively early in the Specimen 3 configuration. In the uniaxial tensile region (Specimen 1), the curve reached a major strain level of 0.2693, while in the multi-axial tension paths within the positive minor strain zone (Specimens 6 and 7), the limit values converged within the 0.3396–0.3444 major strain range.

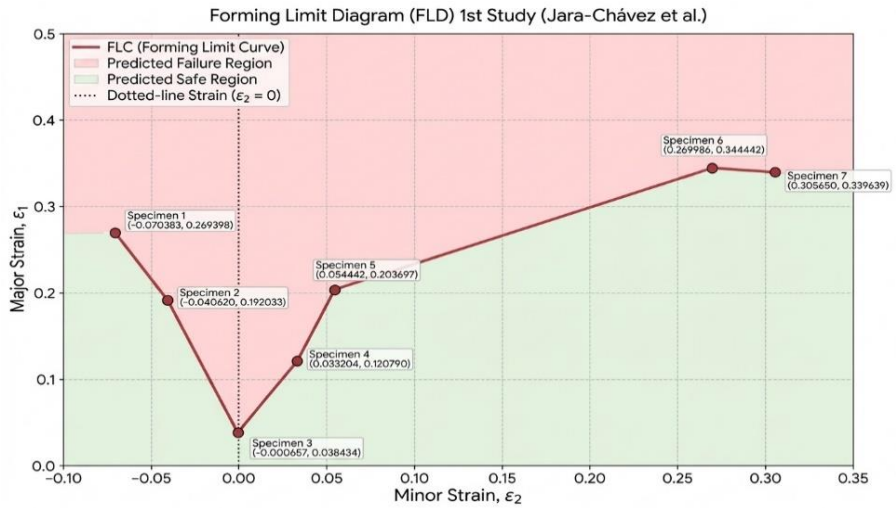



Figure 6. Forming limit diagram of sheet metal specimens in dataset 1 (Jara-Chávez et al.)

Upon evaluating the diagram for the second dataset, it was observed that despite a lower true yield strength of 150.226 MPa, the $FLC_0$ threshold reached an elevated major strain value of 0.0803. This behavior is associated with the higher strain-hardening exponent (n = 0.154), which helps delay local thinning trends and expands the forming limit strain under the adopted parameters. This alloy configuration, within the numerical model constraints, appeared to delay plastic instability at the near-plane strain limit. In the negative-minor-strain region associated with

tensile loading paths (Specimen 1), the curve showed a rise near a major strain of 0.3208, while in the biaxial tensile region (Specimens 6 and 7), it followed a stable trend near a major strain level of 0.3391.

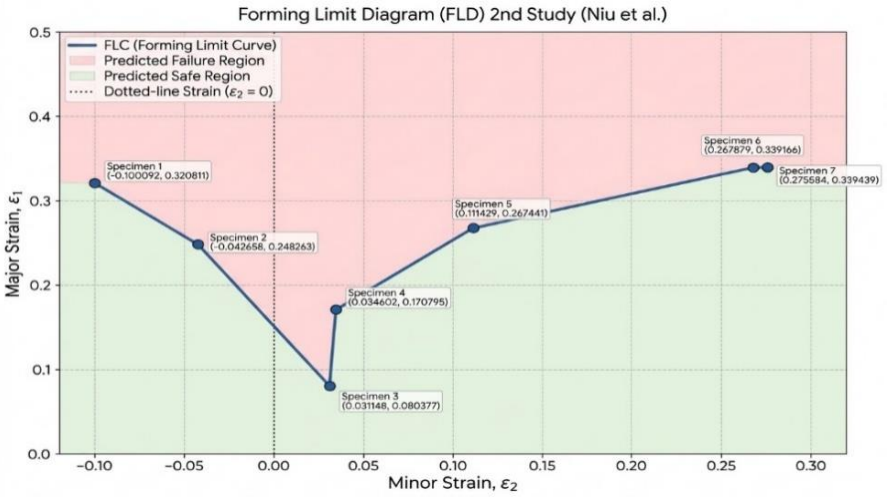



Figure 7. Forming limit diagram of sheet metal specimens in dataset 2 (Niu et al.)

In the FLD curve for the third dataset, a higher localized resistance to thinning around the critical near-plane-strain path was obtained, which is linked to the balance between moderate yield strength and directional plastic anisotropy. The critical threshold for in-plane strain reached a major strain value of 0.1113, thereby offering a balanced performance profile within the scope of the study. On the uniaxial loading path to the left of the curve (Specimen 1), the model exhibits a capability to delay the predicted onset of plastic instability by reaching a major strain limit of 0.3709; whereas on the biaxial stress paths on the right side (Specimens 6 and 7), it balanced within the major strain limit range of 0.3263–0.3445.

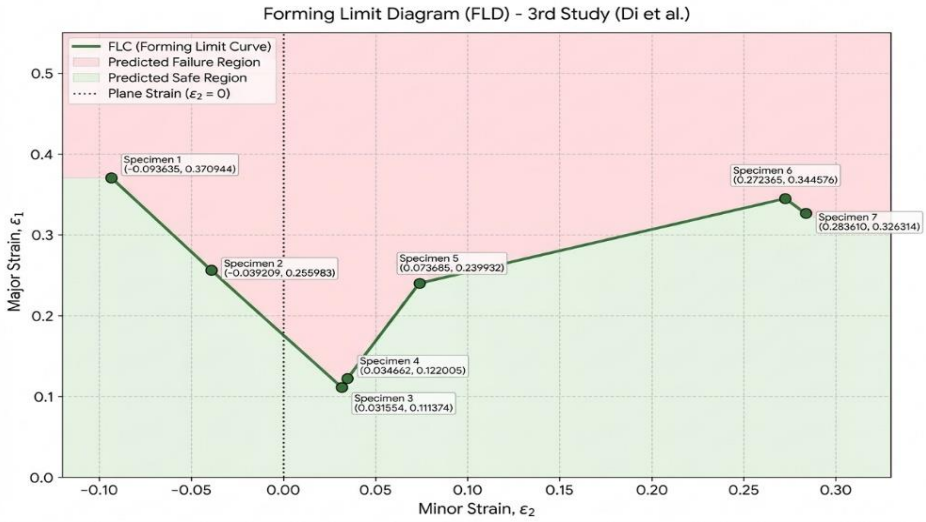



Figure 8. Forming limit diagram of sheet metal specimens in dataset 3 (Di et al.)

Referring to Figure 9, which presents a combined evaluation of the formability limit diagrams from all three independent studies, the results indicate that variations in alloying elements and the derived model coefficients have the capacity to selectively influence different deformation paths. Distinct vertical variations between the models reemerged in the negative-minor-strain region associated with tensile loading on the left side of the curves and in the near-plane strain regions at the center; suggesting that the predicted forming-limit curves differ across the material descriptions, although the isolated effects of composition cannot be independently determined from the present comparisons. In contrast, when moving to the fully biaxial strain field on the right side of the diagram—which contains positive minor strains—it was observed that all three curves departed from their instantaneous deviations in the intermediate strain band and converged, forming a common plateau in the 0.32–0.34 major strain band.

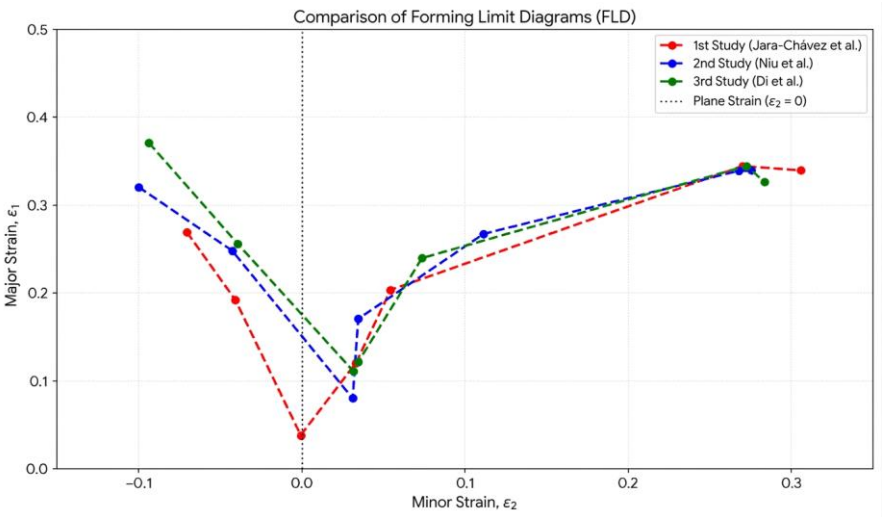



Figure 9. Comparison of FLD graphs for the three reference data points

This morphological convergence at the balanced biaxial stretching domain suggests that the geometric constraints of the tooling, alongside shared numerical assumptions such as the identical plastic localization criterion and flow stress extrapolation limits, establish a stabilized bounding profile; conversely, it suggests that elementary variations establish a distinct protective limit on planar strain and uniaxial deep-drawing stability. Consequently, these observed deviations across the deeper strain paths suggest that the macroscopic formability limits remain closely bounded by the primary hardening inputs established during the initial data reduction. Given that the underlying constitutive calibration incorporates total fracture boundaries due to bulk literature constraints, these resulting multi-axial profiles indicate preliminary computational trends within the adopted assumptions rather than validated physical limits. This qualified approach provides an early-stage screening envelope to evaluate relative plastic instability risks, emphasizing that the numerical forming limit curves serve as conceptual design boundaries pending direct experimental rolling texture validation.

For the evaluated specimen geometries, the incremental strain histories experience structural path deviations during the early stages of the stretching procedure. These early-stage path non-linearities are associated with dynamic multiaxial contact shifts and blank holder friction gradients over the hemispherical dome apex. Consequently, the deformation trajectories do not maintain ideal structural proportionality throughout the complete cycle, suggesting that the virtual threshold estimations should be interpreted as outcomes bounded by these inherently complex and non-proportional strain path evolutions.

To conceptually evaluate the mathematical boundary conditions of the synthetic model, a preliminary qualitative sensitivity discussion was conducted by introducing hypothetical perturbations to the Lankford coefficients and varying the orientation angle parameter between 60° and 75°. These mathematical variations were performed strictly as an early-stage exploratory exercise to analyze how the Hill48 yield surface reacts under changed anisotropic flow potentials within the plane-stress constraints. Because these testing boundaries represent assumed mathematical uncertainty parameters rather than statistically established confidence intervals, their outcomes are treated as preliminary computational trends governed by the adopted constitutive assumptions, and no absolute quantitative validation is inferred from these controlled variations.

Furthermore, a distinct physical assessment regarding the correlation between the strain-hardening exponent (n) and the true strain indicators listed in Table 2 must be addressed. According to the classical Considère stability criterion, the onset of diffuse necking under homogeneous uniaxial tension approximately coincides with the condition εp ≈ n. The derived parameters indicate that the total true strains reported from the source literature (0.2358, 0.854, and 0.307) significantly exceed the analytical hardening exponents (0.063, 0.154, and 0.080). This macro-scale divergence stems from the fact that the benchmark next-generation Zn–Ag–Cu alloy processing configurations activate extensive post-uniform flow regimes—such as grain boundary sliding in superplastic cold-rolled sheets or continuous dynamic recrystallization under high-ratio hot extrusions—allowing the material to sustain high fracture elongations long after initial local instability is triggered. Implementing a pure Hollomon power-law framework across these coordinates introduces specific numerical characteristics governed by the adopted constitutive curves. Rather than guaranteeing absolute engineering safety margins or definitive physical lower bounds, the resulting multi-axial flow trajectories must be interpreted strictly as preliminary computational predictions under the adopted parameters. These bounded curves outline initial screening thresholds within the virtual environment, emphasizing that physical component formability remains dependent on empirical validations under actual stamping states.

To capture the directional mechanics of the underlying hexagonal close-packed (HCP) matrix, the orientation angle parameter (Φ = 67.5 degrees) was implemented strictly as a hypothetical baseline parameter within the planar harmonic framework. It is explicitly recognized that crystallographic texture evolution is a statistical distribution of grain orientations heavily governed by thermomechanical processing histories, including distinct extrusion and cold-rolling routes. Because direct experimental microstructural orientation measurements—such as electron backshift diffraction (EBSD) or X-ray diffraction (XRD) pole figures—were outside the scope of this preliminary study, this angular value represents an idealized, hypothetical orientation parameter designed to calibrate the anisotropic flow surface equations. Consequently, this assumption serves as a conceptual numerical baseline rather than an invariant physical property of the specific processed alloy sheets, and its descriptive limits are bounded by the adopted constitutive definitions.

It may be noted that the reported formability trends are evaluated using a uniform 3.0 mm solid-shell discretization selected to secure macro-scale continuous flow stability within the implicit solver. In localized tracking procedures, reducing grid spaces to overly refined configurations might introduce premature localized strain concentration artificial shifts, potentially masking the pure material anisotropy response. Consequently, the chosen spatial resolution balance is characteristically adjusted to support stable deformation path evaluations while maintaining convergence relative to the sheet thickness baseline, suggesting that the virtual outcomes are treatable as baseline numerical indicators governed by these established continuous grid parameters.

**4. Conclusion**

The multiaxial plastic deformation limits and plastic instability tendencies of next-generation ternary Zn–Ag–Cu alloy sheets were evaluated within the framework of preliminary computational models. By tracking virtual Nakajima stretching configurations under the adopted baseline assumptions, the numerical trends indicate that variations in alloy configurations and estimated anisotropic descriptions appear more visible within uniaxial deep drawing and near-plane strain paths. Conversely, under biaxial tension domains, the simulated curves tend to converge toward closer limit regions, which is associated with the dominant geometric boundary constraints of the tooling.

It is recognized that this predictive framework represents a conceptual verification of the numerical implementation rather than a physical validation of specific Zn–Ag–Cu material dynamics. While the calculated forming limit profiles outline a V-shaped morphology consistent with general sheet-forming principles, these trajectories are treated as tentative computational trends rather than experimental material properties. Due to the limited availability of independent multiaxial experimental coupon tests for these specific alloy configurations in existing literature, the derived boundaries are presented as a preliminary screening tool to estimate potential local instability tendencies.

Furthermore, the analytical approximations used to approximate macro-scale behavior based on crystal lattice geometry serve as idealized assumptions within the model. The resulting synthetic cards provide a qualitative baseline to evaluate directional thinning tendencies characteristic of hexagonal close-packed zinc matrices under multiaxial loading. Within this context, the variations suggest that the predicted forming-limit boundaries are coupled with the selected computational options and the specific localization tracking methods. Consequently, these quantitative outcomes are interpreted as preliminary indicators, confirming that definitive material formability limits remain subjected to further exploration pending future multi-directional experimental sheet stretching validation.

## Author Contributions

Atilla Uğurlu: Conceptualization, Methodology, Software, Formal Analysis, Investigation, Data Curation, Visualization, Writing – Original Draft.

Sinan Sezek: Conceptualization, Methodology, Supervision, Validation, Writing – Review & Editing.

## Funding

This research received no external funding.

## Data Availability Statement

The data presented in this study are available from the corresponding author upon reasonable request.

## Conflict of Interest Statement

The authors declare that there is no conflict of interest. They have no known competing financial interests or personal relationships that could have appeared to influence the work reported in this paper.

## References

[1.] Pola, A., Tocci, M., Goodwin, F.E., Review of Microstructures and Properties of Zinc Alloys. Metals 10 (2020) 253.

[2.] Boukalová, A., Kubásek, J., Nečas, D., Minárik, P., Donik, Č., Dvorský, D., Vojtěch, D., Michalová, A., Godec, M., Paulin, I., Harmonizing microstructures and enhancing mechanical resilience: Novel powder metallurgy approach for Zn-Mg alloys. Journal of Materials Research and Technology 31(2024)2807–2819.

[3.] Heiss, A., Thatikonda, V.S., Richter, A., Schmitt, L.Y., Klotz, U.E., Development, Processing and Aging of Novel Zn-Ag-Cu Based Biodegradable Alloys. Materials 16(2023)3198.

[4.] Ali, B., R., R., Karmakar, S., Zinc alloys in biomedical implants: A review of mechanical performance and corrosion behavior. Next Materials, 13 (2026) 102608.

[5.] Shi, Z.Z., Gao, X.X., Zhang, H.J., Liu, X.F., Li, H.Y., Zhou, C., Yin, Y.X., Wang, L.N., Design biodegradable Zn alloys: Second phases and their significant influences on alloy properties. Bioactive Materials 5(2020)210–218.

[6.] Aghajani, S., Alizadeh, R., Severe plastic deformation of Zn and Zn-based alloys. Journal of Materials Research and Technology 33 (2024) 6508–6533.

[7.] Chen, Y., Zhao, S., Wang, Y., Liu, Y., Hu, Z., Qian, D., Han, X., Wang, H., Lin, J., Hua, L., Advanced forming technologies for integrated metal components with extreme size and structure: State-of-the-art and perspectives. Chinese Journal of Mechanical Engineering 39(2026)100027.

[8.] Lu, Y., Fu, Y., Liu, Y., Dai, Y., Yan, Y., Yu, K., Effects of Extrusion and Rolling Processes on the Microstructure and Mechanical Properties of Zn-Li-Ag Alloys. Metals 12(2022)520.

[9.] Jarzębska, Y., Maj, Ł., Bieda, M., Chulist, R., Wojtas, D., Wątroba, M., Janus, K., Rogal, Ł., Sztwiertnia, K., Dynamic Recrystallization and Its Effect on Superior Plasticity of Cold-Rolled Bioabsorbable Zinc-Copper Alloys. Materials 14(2021)3483.

[10.] Ardakani, M.S., Kampe, S.L., Drelich, J.W., Flow stress stabilization of Zn-Cu-Mn-Mg alloys using thermomechanical processing. Materials Characterization 188(2022)111928.

[11.] Khafizova, E., Fakhretdinova, E., Islamgaliev, R., Polenok, M., Sitdikov, V., Yilmazer, H., Effect of Plastic Deformation on the Structure and Mechanical Properties of the Zn-4Ag-1Cu Zinc Alloy. Materials 16(2023)4646.

[12.] Schlosser, F., Signorelli, J., Leonard, M., Roatta, A., Milesi, M., Bozzolo, N., Influence of the strain path changes on the formability of a zinc sheet. Journal of Materials Processing Technology 271(2019)101–110.

[13.] Rubešová, K., Rund, M., Rzepa, S., Jirková, H., Jeníček, Š., Urbánek, M., Kučerová, L., Konopík, P., Determining Forming Limit Diagrams Using Sub-Sized Specimen Geometry and Comparing FLD Evaluation Methods. Metals 11(2021)484.

[14.] Lumelskyj, D., Rojek, J., Lazarescu, L., Banabic, D., Determination of forming limit curve by finite element method simulations. Procedia Manufacturing 27(2019)78–82.

[15.] Dikmenli, S., Alternative numerical simulation approach for obtaining FLC/FLD. Eurasian Journal of Science Engineering and Technology 4(2023)001–009.

[16.] Deng, Z., McGuire, J. P., Development of novel forming limit curve testing method. IOP Conference Series: Materials Science and Engineering 418(2018)012049.

[17.] Wang, Y.; Zhang, C. The determination of friction coefficient in Nakazima test and its application in predicting FLCs with modified M-K model. IOP Conference Series: Materials Science and Engineering 2020, 967, 012056

[18.] International Organization for Standardization. Metallic Materials—Sheet and Strip—Determination of Forming-Limit Curves—Part 2: Determination of Forming-Limit Curves in Laboratory; ISO Standard No. 12004-2; ISO: Geneva, Switzerland, 2008

[19.] Jansen, Y.; Logé, R. E.; Milesi, M.; Massoni, E. An anisotropic stress-based criterion to predict the formability and the fracture mechanism of textured zinc sheets. Journal of Materials Processing Technology 2013, 213, 851–855.

[20.] Jara Chávez, G.; Amaro Villeda, A.; Campillo Illanes, B.; Ramírez-Argáez, M.; Gonzalez-Rivera, C. Effect of Ag and Cu content on the properties of Zn-Ag-Cu-0.05Mg alloys. Metals 2024, 14, 740.

[21.] Niu, K.; Zhang, D.; Qi, F.; Lin, J.; Dai, Y. The effects of Cu and Mn on the microstructure, mechanical, corrosion properties and biocompatibility of Zn–4Ag alloy. Journal of Materials Research and Technology 2022, 21, 4969–4981.

[22.] Di, T.; Xu, Y.; Liu, D.; Sun, X. Microstructure, Mechanical Performance and Anti-Bacterial Activity of Degradable Zn-Cu-Ag Alloy. Metals 2022, 12, 1444.

[23.] Montes, J. M., Ternero, F., On the calculation of the density of multi-component solid solutions. Intermetallics 185(2025)108924.

[24.] Hill, R., The elastic behaviour of a crystalline aggregate. Proceedings of the Physical Society. Section A 65(1952)349–354.

[25.] Callister, W. D., Rethwisch, D. G., 2018. Materials Science and Engineering: An Introduction (10th ed.), Wiley. Hoboken, ABD, 565-590.

[26.] Meyers, M. A., Chawla, K. K., 2009. Chapter 16: Composite Materials. Mechanical Behavior of Materials (2nd ed.), Cambridge University Press. Cambridge 107-115, 776-779.

[27.] Beer, F., Johnston, E. R., Dewolf, J. T., Mazurek, D. F., 2012. Chapter 2: Stress and Strain-Axial Loading. Mechanics of Materials (6th ed.), McGraw-Hill. New York, 103.

[28.] Hosford, W. F. Mechanical Behavior of Materials; Cambridge University Press: Cambridge, 2010; pp. 92–95.

[29.] Dieter, G. F., Mechanical metallurgy: SI metric edition (Bölüm 4: Concepts of crystal geometry). McGraw-Hill Book Company 1988(107, 187, 673).

[30.] King, H. W. Quantitative size-factors for metallic solid solutions. Journal of Materials Science 1966, 1, 79–90.

[31.] Chen, C.; Fan, S.; Niu, J.; Huang, H.; Jin, Z.; Kong, L.; Zhu, D.; Yuan, G. Alloying design strategy for biodegradable zinc alloys based on first-principles study of solid solution strengthening. Materials & Design 2021, 204, 109676.

[32.] Callister, W. D.; Rethwisch, D. G. Materials Science and Engineering: An Introduction, 9th ed.; John Wiley & Sons: New York, 2014; pp. 82–84, 111–114, 174, 221–222.

[33.] Kocks, U. F.; Tomé, C. N.; Wenk, H. R. Texture and Anisotropy: Preferred Orientations in Polycrystals and Their Effect on Materials Properties; Cambridge University Press: Cambridge, 1998; Chapter 8, pp. 331–334.

[34.] Nabarro, F. R. N., Fifty-year study of the Peierls-Nabarro stress. Materials Science and Engineering: A 234–236(1997)67–76.

[35.] Kishida, K., Kim, J. G., Nagae, T., Inui, H., Experimental evaluation of critical resolved shear stress for the first-order pyramidal c+a slip in commercially pure Ti by micropillar compression method. Acta Materialia 196(2020)168–174.

[36.] Cullity, B. D., Appendix 3. Elements of X-Ray Diffraction (2nd ed.). Addison-Wesley Publishing Company 1978(501).

[37.] Nicoletti, E. A., Roatta, A., Marinelli, L. P., Signorelli, J. W., Celentano, D. J., Experimental and numerical analysis of prestrain on the formability of Zn-Cu-Ti alloy zinc sheet. Metals 12(2022)1095.

[38.] Yang, B., Chapter 5: Static Analysis of Linearly Elastic Bodies. Stress, Strain, and Structural Dynamics: An Interactive Handbook of Formulas, Solutions, and MATLAB Toolboxes (1st ed.). Academic Press 2005(143).

[39.] Hosford, W. F., Caddell, R. M., Metal Forming: Mechanics and Metallurgy. Cambridge University Press 2007(210, 215)

[40.] Hill, R., A theory of the yielding and plastic flow of anisotropic metals. Proceedings of the Royal Society of London. Series A. Mathematical and Physical Sciences 193(1948)281–297.

[41.] Shi, L.; Yang, Y.; Hou, B.; Gu, W.; Zhao, H.; Feng, Y.; Hang, Z. A new method for determining necking of sheet metal based on main strain topography. Coatings 2024, 14, 765.

[42.] Hill, R. Theoretical plasticity of textured aggregates. Math. Proc. Camb. Phil. Soc. 1979, 85, 179–191.

## How to Cite This Article

Uğurlu, A., Sezek, S., Numerical Investigation of Forming Limits in Zn–Ag–Cu-Based Alloy Sheets Using Estimated Anisotropic Constitutive Properties, Brilliant Engineering, 1(2027), 41215.
https://doi.org/10.36937/ben.2027.41215